ACS APPLIED MATERIALS & INTERFACES

www.acsami.org

Research Article

Quasi-Stable Salt Gradient and Resistive Switching in Solid-State Nanopores

Iat Wai Leong, Makusu Tsutsui,* Sanae Murayama, Tomoki Hayashida, Yuhui He, and Masateru Taniguchi

Cite This: *ACS Appl. Mater. Interfaces* 2020, 12, 52175−52181

Read Online

ACCESS | Metrics & More | Article Recommendations | Supporting Information

ABSTRACT: Understanding and control of ion transport in a fluidic channel is of crucial importance for iontronics. The present study reports on quasi-stable ionic current characteristics in a SiN_x nanopore under a salinity gradient. An intriguing interplay between electro-osmotic flow and local ion density distributions in a solid-state pore is found to induce highly asymmetric ion transport to negative differential resistance behavior under a 100-fold difference in the cross-membrane salt concentrations. Meanwhile, a subtle change in the salinity gradient profile led to observations of resistive switching. This peculiar characteristic was suggested to stem from quasi-stable local ion density around the channel that can be switched between two distinct states via the electro-osmotic flow under voltage control. The present findings may be useful for neuromorphic devices based on micro- and nanofluidic channels.

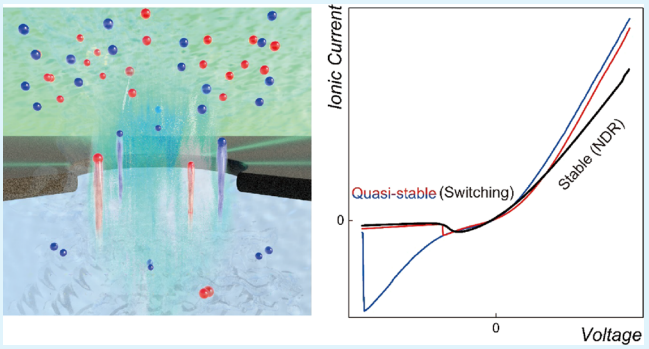

KEYWORDS: *electro-osmosis, ion transport, negative differential resistance, salt gradient, resistive switching*

INTRODUCTION

Ion transport in a fluidic channel has been intensively studied for promising applications including energy harvesters,[1−5] iontronics,[6−10] artificial neurons,[11] and single-molecule sensing.[12,13] It implements electric field-driven ion and mass transport in a confined space, wherein electrostatics and fluid dynamics reflect rich properties of the wall surface to induce pronounced ion selectivity and the associated unique ionic current characteristics that cannot be expected in bulk systems. According to this principle, nanofluidic devices demonstrated a variety of ion transport properties such as ionic current rectification (ICR) and negative differential resistance (NDR)[14,15] via geometric structure engineering,[17] membrane material designs,[18,19] and molecular functionalizations[10,20−22] to provide high-density surface charge to the walls[14] and increase the surface-to-volume ratio of fluidic channels. The surface effects were, however, known to be effective only in a small channel of sub-Debye length size because of screening of the electrostatic field at the wall by the electrolyte ions.

In contrast, a salinity gradient across a conduit was recently found to enable asymmetric ion transport with respect to bias voltage polarity[15,17,23] even in channels of micrometer-scale diameter.[24] The peculiar ionic current characteristics were explained by voltage-driven modulation of the cross-membrane salt gradient under the influence of diffusio-osmotic and electro-osmotic fluid flow.[25−30] For instance, Rabinowitz et al.[23] observed ICR in 25 nm diameter glass pipettes with an ion concentration ratio between 10 and 21, which was ascribed to electro-osmosis-induced Eddy current driving more or less concentrated solution into the channel in a voltage-dependent manner.[23] Moreover, NDR was reported by Lin et al.[15] for 100 and 400 nm-sized nanopores in a 12 μm thick PET membrane under a concentration ratio between 10 and 1000, where the authors found the influence of the interplay between electro-osmotic and diffusio-osmotic contributions on the asymmetric ion transport characteristics.[15] Whereas these literatures found the rectifying behavior in fluidic channels having a relatively high length-to-diameter aspect ratio structure, we herein report that such electrokinetic effects are observable even in low thickness-to-diameter aspect-ratio micropores where any surface charge effects were anticipated to become negligibly small under the orders of magnitude larger space given for the ion transport with respect to the Debye length. Surprisingly, we found more pronounced electro-diffusio-osmotic contributions in the shallow channels that led to anomalous ionic current characteristics from NDR to resistive switching.

Received: August 28, 2020
Accepted: October 22, 2020
Published: November 5, 2020

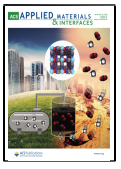

https://dx.doi.org/10.1021/acsami.0c15538
ACS Appl. Mater. Interfaces 2020, 12, 52175−52181

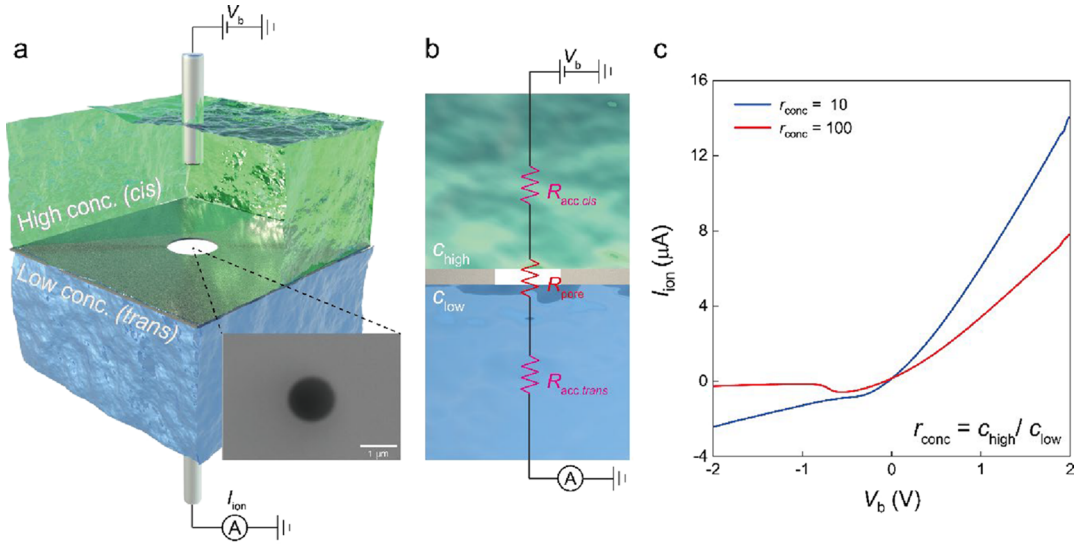

Figure 1. Measurements of the ionic current through a solid-state pore in a thin dielectric membrane. (a) Schematic model of a SiN_x pore, both sides filled with either electrolyte buffers of high (green) or low (blue) ionic concentration buffers. The voltage V_b is applied to the pore at the *cis* chamber, and the resulting ionic current I_{ion} is measured at the other side using a pair of Ag/AgCl electrodes. The inset shows a scanning electron micrograph of the 1 μm-sized micropore. (b) Equivalent circuit model. $R_{acc.cis}$ and $R_{acc.trans}$ are the access resistance in the *cis* and *trans* compartments, respectively. R_{pore} is the pore resistance inside the pore. (c) Typical current−voltage characteristics of a low thickness-to-diameter aspect-ratio pore (1 μm diameter and 50 nm thick) under the moderate (blue curve) and large (red curve) salt gradients. r_{conc} is the ratio of the bulk salt concentrations at the *cis* and *trans*.

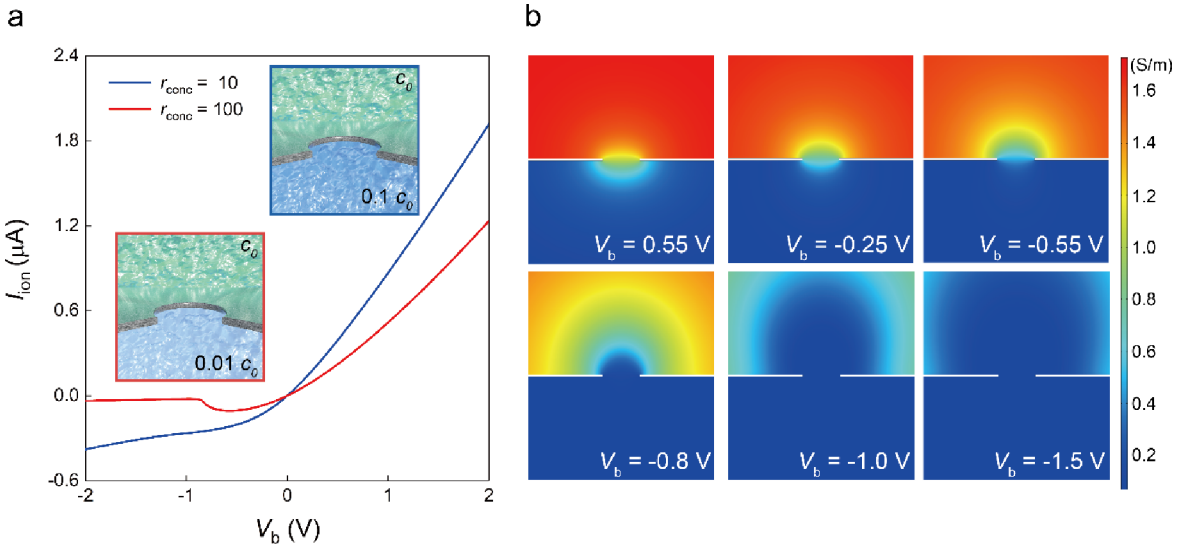

Figure 2. Finite element analyses of ion transport in the salt gradient-applied low-aspect-ratio pore. (a) Calculated ionic current I_{ion} versus cross-membrane voltage V_b characteristics of a 1 μm diameter and 50 nm thick SiN_x pore. c_0 = 137 mM denotes the concentration of Na^+ and Cl^- in the electrolyte buffer used. Blue and red curves are the results when r_{conc} is 10 and 100, respectively. (b) Cross-sectional views of the two-dimensional conductivity around the pore under different V_b.

RESULTS AND DISCUSSIONS

A 1 μm diameter pore was fabricated in a 50 nm thick SiN_x membrane by electron beam lithography and reactive ion etching. A pair of Ag/AgCl electrodes were used for measurements of the ionic current (I_{ion}) versus cross-membrane bias voltage (V_b) characteristics in phosphate-buffered saline (PBS). The ionic strength was varied by diluting the buffer with ultrapure water from 10 c_0 to 0.01 c_0, where c_0 = 137 mM is the concentration of Na^+ and Cl^- in 1 × PBS. A salt gradient was formed across the pore by filling the *cis* and *trans* chambers with PBS of high (c_{high}) and low (c_{low}) ion concentrations (Figure 1a). Hereafter, we use $r_{conc} = c_{high}/c_{low}$ to describe the salinity difference.

Under a uniform ion concentration condition (r_{conc} = 1), the ionic resistance R_{total} complied with an analytical expression of $R_{total} = R_{acc} + R_{pore}$, where R_{acc} and R_{pore} are, respectively, the resistance outside and inside the pore (Figure 1b). Note that for the present channel having a low thickness-to-diameter aspect ratio structure, R_{acc} is an order of magnitude larger than R_{pore}.[31−33] Whereas I_{ion}−V_b characteristics were observed to be linear at r_{conc} = 1, we found diode behavior when adding a 10-fold difference between c_{high} and c_{low} (r_{conc} = 10) with a rectification ratio of 4.6 at ±1 V. This ion transport asymmetry

https://dx.doi.org/10.1021/acsami.0c15538
ACS Appl. Mater. Interfaces 2020, 12, 52175−52181

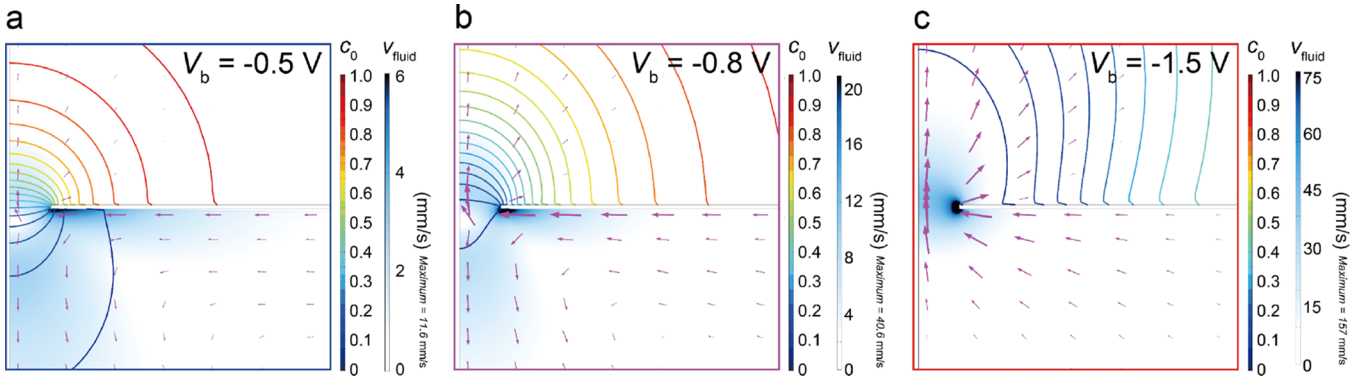

Figure 3. Voltage-dependent ion concentration distributions. (a–c) Simulation results of ion concentration isosurfaces around a 1 μm diameter and 50 nm thick SiN_x pore under (a) V_b = −0.5 V, (b) −0.8 V, and (c) − 1.5 V. Blue contrasts and purple arrows depict the electro-diffusio-osmosis-driven fluid flow speed and directions, respectively.

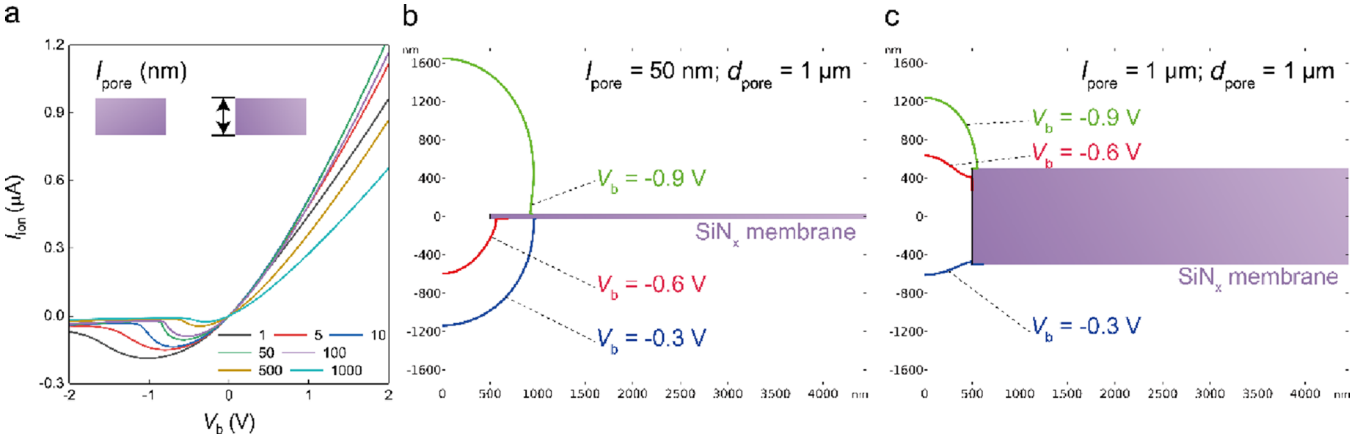

Figure 4. Pore structure-dependent ionic current characteristics. (a) COMSOL-simulated I_{ion}–V_b characteristics of a 1 μm diameter pore in a SiN_x membrane of various thicknesses from 1000 to 1 nm ($c_{bulk,cis}$ = 1 c_0, $c_{bulk,trans}$ = 0.01 c_0). (b, c) Moving ion concentration isosurface at 0.1c_0 under voltage sweep for (b) 50 nm and (c) 1 μm thick pores.

was ascribed to voltage-dependent salt gradient modulations by the electro-osmotic flow (EOF) that lowers (enhances) the effective ion concentration around the micropore under the positive (negative) V_b.[17,18] The plots were also confirmed to be reproducible under repeated bias ramps, suggesting reversible ion distributions under the V_b-driven hydrodynamic control.

Enlarging the salt gradient to r_{conc} = 100 (red curve in Figure 1c), I_{ion}–V_b characteristics became more asymmetric with the rectification ratio as high as 24.8. Unexpectedly, it also revealed NDR behavior at around V_b = −0.56 V. Considering the predominant role of EOF in the ion flow asymmetry,[16] this feature can be naturally interpreted as a consequence of the augmented electro-diffusio-osmotic flow at critical V_b that diluted the local ion concentration at the pore orifice and thereby led to a rapid increase in R_{acc}.

To theoretically verify the mechanism underlying the NDR behavior, we performed finite element analyses of the cross-membrane ion transport by solving time-independent Poisson–Nernst–Planck and Navier–Stokes equations in a framework of a finite element method using COMSOL. The model is constructed with a disk-shaped pore having a diameter (d_{pore}) of 1 μm in a SiN_x membrane of 50 nm thickness (l_{pore}).[28,30] The entire surface of the membrane was considered as negatively charged at −15 mC/m^2. The simulation reproduced NDR and ICR when setting r_{conc} = 100 (c_{cis} = 1 c_0; c_{trans} = 0.01 c_0) and r_{conc} = 10 (c_{cis} = 1 c_0; c_{trans} = 0.1 c_0), respectively, which are in good agreement with the experimental results. Further calculations revealed an ICR-to-NDR transition point at around r_{conc} = 14 (Figure S1).

The simulations also elucidated the important role of the pore wall surface charge (Figure S2). It is found that decreasing the amount of negative charges on the membrane led to a weaker NDR. They also elucidated the profound influence of the entire membrane surface, where we observed no NDR behavior in cases when only a part of the surface was set to be charged (Figure S3). This was confirmed in experiments as well where we observed disappearance of the NDR feature when we reduced the amount of negative charges on the wall surface by coating the SiN_x pore with 20 nm thick Al_2O_3 (Figure S4). These results manifest a crucial role of the surface charge in the salt gradient-derived asymmetric ion transport characteristics.

Moreover, mapping the local ion density at around the pore (Figure 2), we detected a rapid decrease in the cation and anion concentrations when lowering V_b below −0.55 V. This tendency is in qualitative accordance with the expected influence of the EOF streaming from *trans* to *cis* to make R_{acc}, or equivalently R_{total} for the present low-aspect-ratio micropore, larger by diluting the ions in the pore region at V_b < −0.55 V. NDR can thus be explained as a consequence of the faster voltage-driven fluid speed v_{fluid} in more dilute electrolyte solution due to the extensive surface charge effects under the

https://dx.doi.org/10.1021/acsami.0c15538
ACS Appl. Mater. Interfaces 2020, 12, 52175–52181

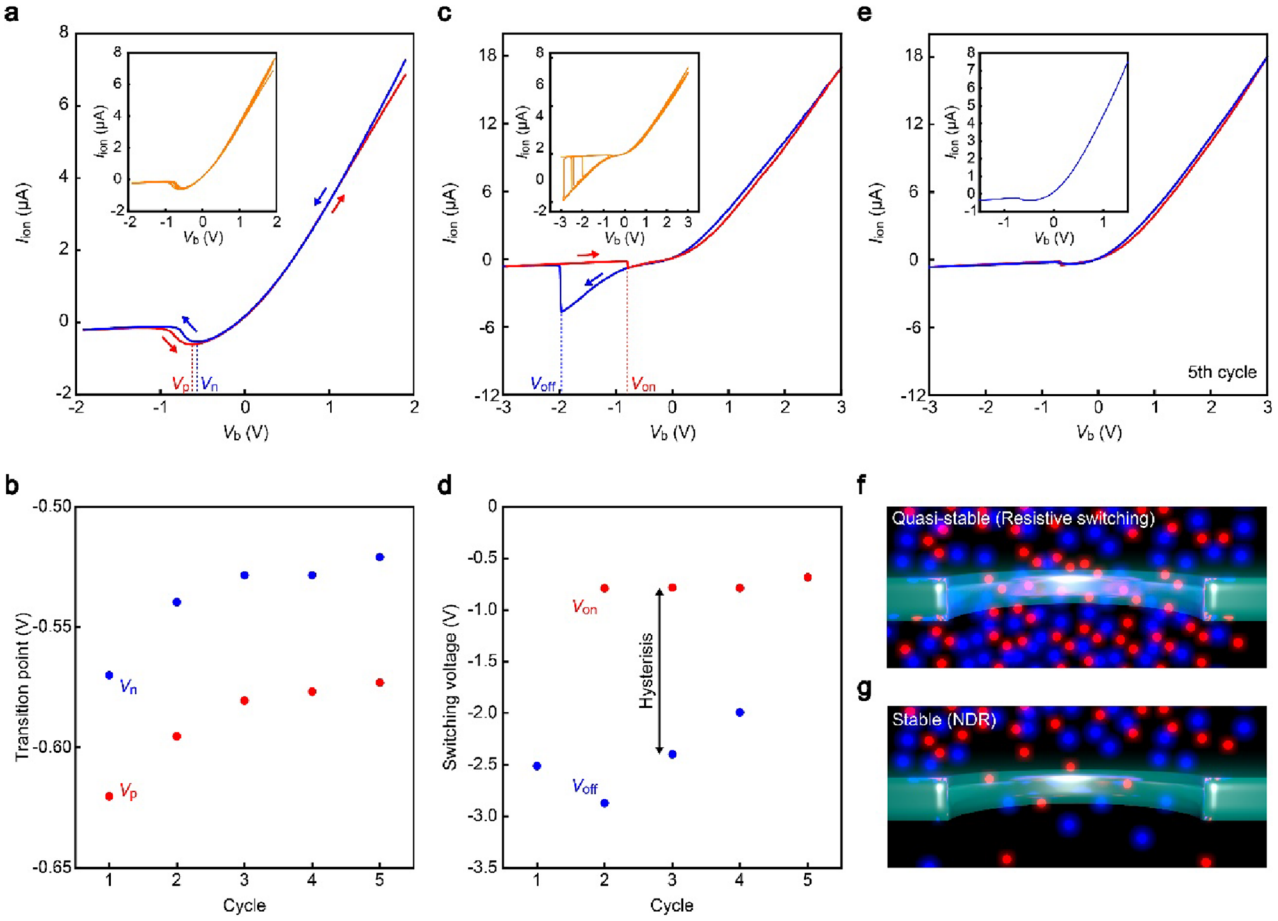

Figure 5. Example of an experimental data set of resistive switching recorded by a 1 μm diameter and 50 nm thick pore when r_{conc} = 100 (*cis* = 10 c_0 and *trans* = 0.1 c_0). (a) Repeated I_{ion}−V_b measurements with little hysteresis under positive and negative sweeps. The ionic current changed smoothly under the V_b sweeps. The inset shows the results of five cycles of the I_{ion}−V_b measurements. (b) Voltage at I_{ion} minima in (a) during the positive (V_p) and negative (V_n) voltage sweeps. (c) I_{ion}−V_b curves with large hysteresis. The inset shows the results of five cycles of the measurements. The conductance tends to jump from high to low states during the voltage sweeps in a negative direction at V_{off} (blue). Subsequently, the conductivity was reset to the original state at V_{on} when scanning back the voltage (red). (d) Change in V_{on} and V_{off} during several cycles of V_b sweeps, demonstrating smaller hysteresis by repeating the voltage scans. (e) Result of the fifth measurement with no resistive switching but a clear NDR feature (the inset is a magnified view), almost identical to that in (a). (f, g) Schematic models describing (f) symmetric and (g) asymmetric ion density distributions responsible for the stable NDR and quasi-stable resistive switching behaviors.

longer screening length,[17] which eventually causes the ionic current to decrease with increasing $|V_b|$.

How about the EOF velocity then? Figure 3 shows the fluid velocity contours at V_b = −0.5 V, −0.8 V, and − 1.5 V under r_{conc} = 100. At −0.5 V, the flow speed is fast only near the wall surface because of the short Debye length under the high in-pore ion concentration condition, as depicted by the ion density isosurfaces (Figure 3a). Enlarging the voltage to −0.8 V (Figure 3b), on the other hand, the flow speed suddenly becomes more significant in the entire channel. This characteristic feature is revealed as stemming from the concomitant weakening of the diffusio-osmotic effect for the stronger EOF, which makes the ion density in the channel more homogeneous (Figure S5).[15] It is perhaps this self-catalytic effect that depletes ions at the channel openings more significantly than the current gain by larger $|V_b|$, thus bringing about NDR at the specific range of negative voltage. Meanwhile, further voltage sweep (Figure 3c) led to a linear decrease in I_{ion} with a slope close to $1/R$ under c_{high} = c_{low} = 0.01 c_0, as the ion concentration at the *cis* and *trans* orifices is already close to c_{low}. These findings elucidate the important roles of electro-diffusio-osmosis on the highly asymmetric ion transport in low-aspect-ratio pores (Figure S6).

Both the experimental and simulation results consistently suggest the predominant role of EOF in the NDR characteristics. Interestingly, as we increased the channel length l_{pore} from 50 to 1000 nm in the numerical simulations (Figure 4a, see also Figure S7), the NDR features were found to occur at a smaller V_b. This is an intriguing result that reflects the relative influence of R_{acc} and R_{pore} on the pore conductance as well as the different voltage dependences of the EOF. For example, R_{acc} tends to determine the open pore resistance of channels having lower-aspect-ratio structures, which also suggests a more moderate potential gradient at the orifices[34,35] and hence a weaker electric field across the membrane. The resulting EOF during the voltage sweep is therefore expected to be also weak compared to that in the channels of higher-aspect-ratio motifs. Moreover, R_{acc} will be affected only when the ion concentration at the pore orifices is changed appreciably by the fluid flow, which was found to take place only under relatively large voltages in the simulations (Figure 4b). On the other hand, the cross-membrane electric potential tends to drop more sharply inside the channels in the case of higher-

https://dx.doi.org/10.1021/acsami.0c15538
ACS Appl. Mater. Interfaces 2020, 12, 52175−52181

aspect-ratio pores. The resulting stronger EOF induces more facile change in the in-pore ion concentrations by the cross-membrane voltage (Figure 4c). Meanwhile, unlike the shallow channels, such a change in the ion density causes a large impact on the resistance of the high-aspect-ratio conduits because $R_{pore} > R_{acc}$ and hence gives rise to NDR features at lower V_b compared to the lower-aspect-ratio pore counterparts.

How robust are the NDR characteristics? Because the salt gradient was created by merely injecting electrolyte buffers of different dilutions into the *trans* and *cis* chambers without careful manipulations, it was not guaranteed that there will always be a symmetrical ion concentration difference with respect to the SiN_x plane as modeled in the simulations. In fact, whereas stable NDR features were often observed persisting under a number of V_b sweeps, as shown in Figure 5a,b (see also Figures S8 and S9), we also found completely different characteristics demonstrating V_b-controlled bimodal conductance switching (Figure 5c). When this was the case, the $I_{ion}-V_b$ curves showed no clear rectification behavior, keeping the high conductance state even at the negative voltage regime (Figure S8b,c). Meanwhile, the current tended to drop sharply under a large negative voltage. After the switching from high- to low-conductance states at V_{off}, there was another current jump taking place at V_{on} upon reversing V_b to zero. The unipolar conductance switching behavior contained hysteresis characterized by the difference between V_{on} and V_{off}. During several cycles of voltage sweeps, this hysteresis became smaller and eventually disappeared, as displayed in Figure 5d. Thereafter, it showed stable NDR features (Figure 5e) similar to those shown in Figure 5a. The results can be understood as a consequence of nonsymmetrical salt gradient along the pore axis formed before the measurements. More specifically, the fact that the conductance at negative V_b was similar to that in the positive regime suggests a certain extent of intrusion of high-concentration buffer into *cis* during the liquid injection (Figure 5f). However, the salt gradient was presumably quasi-stable under the repeated EOF processes, so that it gradually deformed into the symmetric one after several cycles of $I_{ion}-V_b$ recordings (Figure 5g). This not only proves the robustness of the ionic NDR but also indicates a possible application as memristors[11,36−38] by adding a control over the quasi-stable salt gradient across the membrane.

The presence and absence of resistive switching behavior are thus attributed to the varying initial salt gradient conditions that were not controllable under the experimental procedure used where the high-concentration electrolyte buffer was injected to one side of the membrane and then the low-concentration one to the other side using a syringe. As a consequence, the ion distribution around the micropores was presumably asymmetric in some cases at the first point, resulting in the resistive switching behavior, as shown in Figure 5c. Otherwise, when the ion distribution was symmetric, the $I_{ion}-V_b$ curves showed stable NDR characteristics under the repetitive voltage sweeps (Figure 5a).

CONCLUSIONS

In summary, we observed asymmetric ion transport characteristics in a low-aspect-ratio solid-state pore under the applied 100-fold salt concentration difference across the membrane. We found mutual roles of diffusio-osmosis and electro-osmosis in rapidly decreasing the local ion density at the channel orifices under negative voltage sweeps and thereby causing NDR behavior. This characteristic was also suggested to take place only under a symmetric salt gradient across the channel. Otherwise, the electro-diffusio-osmotic effects induce conductance switching until the asymmetric local ion density distribution becomes symmetric via EOF under the repeated voltage ramps. The present results may provide a guide to design micro- and nanofluidic memristors.

METHODS

Fabrications of Solid-State Pores. The micropore fabrication processes were based on electron beam lithography and reactive-ion etching, as reported in previous literatures.[39] A 50 nm thick SiN_x-coated silicon wafer was used as a substrate. By two-step etching via reactive ion etching using CF_4 and wet etching in KOH solution, a 0.1 mm × 0.1 mm square free-standing membrane was formed. Then, we spin-coated electron beam resist (ZEP520-A) on the membrane. A 1 μm-sized circle was delineated by electron beam lithography (Elionix, WecaS). Using the residual resist layer as a mask, a micropore was drilled by reactive ion etching.

Ionic Current Measurements. The micropore device was pretreated with oxygen plasma to adhere polydimethylsiloxane (PDMS; SYLGARD 184, Dow Corning) blocks created by imprinting on a SU-8/Si mold of microchannels. To obtain the $I_{ion}-V_b$ characteristic data, PBS aqueous solution of $10c_0$ was purchased from Wako co., ltd. without further purification, which was diluted to specific ion concentrations with deionized water (Milli-Q IQ 7000 ultrapure water system). Pouring the buffer into the *cis* and *trans* using a syringe, the cross-membrane ionic current was measured using a pair of Ag/AgCl electrodes. Here, bias voltage V_b was swept from −1.5 to +1.5 V (−3 to +3 V for the measurement given in Figure 5) with 0.05 V steps, and I_{ion} was recorded using Keithley 6487 (Keithley). All the experiments were performed at room temperature in a Faraday cage.

Finite Element Simulations. The geometry and boundary conditions used in finite element simulations are shown in Figure S10 and Table S1. A cylindrical pore was defined in a 2D axisymmetric model. The cross-pore ion and fluid transport was then simulated by solving Poisson−Nernst−Planck and Navier−Stokes equations using COMSOL 5.4 software with AC/DC and chemical species transport and fluid flow modules. In the model, surface charge at the SiN_x membrane was assumed to be −15 mC/m^2. The chambers at both the sides were modeled as cylinders of 12.5 μm size.[40]

ASSOCIATED CONTENT

Supporting Information

The Supporting Information is available free of charge at https://pubs.acs.org/doi/10.1021/acsami.0c15538.

Simulated roles of salt gradient and pore wall surface charge in the cross-membrane ionic current characteristics; ionic current curves in an Al_2O_3 pore; ion and fluid velocity distributions; pore structure dependence; resistive switching characteristics; and conditions used in the simulations (PDF)

AUTHOR INFORMATION

Corresponding Author

Makusu Tsutsui − *The Institute of Scientific and Industrial Research, Osaka University, Ibaraki, Osaka 567-0047, Japan;* orcid.org/0000-0002-4552-1163; Phone: +81-6-6879-8447; Email: tsutsui@sanken.osaka-u.ac.jp; Fax: +81-6-6875-2440

Authors

Iat Wai Leong − *The Institute of Scientific and Industrial Research, Osaka University, Ibaraki, Osaka 567-0047, Japan;* orcid.org/0000-0002-9100-495X

https://dx.doi.org/10.1021/acsami.0c15538
ACS Appl. Mater. Interfaces 2020, 12, 52175−52181

Sanae Murayama − *The Institute of Scientific and Industrial Research, Osaka University, Ibaraki, Osaka 567-0047, Japan*
Tomoki Hayashida − *The Institute of Scientific and Industrial Research, Osaka University, Ibaraki, Osaka 567-0047, Japan*
Yuhui He − *Wuhan National Laboratory for Optoelectronics, School of Optical and Electronic Information, Huazhong University of Science and Technology, Wuhan 430074, China*
Masateru Taniguchi − *The Institute of Scientific and Industrial Research, Osaka University, Ibaraki, Osaka 567-0047, Japan;* orcid.org/0000-0002-0338-8755

Complete contact information is available at: https://pubs.acs.org/10.1021/acsami.0c15538

Notes

The authors declare no competing financial interest.

■ ACKNOWLEDGMENTS

This work was supported by the Japan Society for the Promotion of Science (JSPS) KAKENHI Grant Number 19 K22108 and 19H00852.

■ REFERENCES

(1) Yeh, L. H.; Chen, F.; Chiou, Y. T.; Su, Y. S. Anomalous pH-Dependent Nanofluidic Salinity Gradient Power. *Small* **2017**, *13*, 1702691.
(2) Cao, L.; Wen, Q.; Feng, Y.; Ji, D.; Li, H.; Li, N.; Jiang, L.; Guo, W. On the Origin of Ion Selectivity in Ultrathin Nanopores: Insights for Membrane-Scale Osmotic Energy Conversion. *Adv. Funct. Mater.* **2018**, *28*, 1804189.
(3) Macha, M.; Marion, S.; Nandigana, V. V. R.; Radenovic, A. 2D Materials as an Emerging Platform for Nanopore-Based Power Generation. *Nat. Rev. Mater.* **2019**, *4*, 588−605.
(4) Hsu, J. P.; Su, T. C.; Peng, P. H.; Hsu, S. C.; Zheng, M. J.; Yeh, L. H. Unraveling the Anomalous Surface-Charge-Dependent Osmotic Power Using a Single Funnel-Shaped Nanochannel. *ACS Nano* **2019**, *13*, 13374−13381.
(5) Xiao, K.; Jiang, L.; Antonietti, M. Ion Transport in Nanofluidic Devices for Energy Harvesting. *Joule* **2019**, *3*, 2364−2380.
(6) Siwy, Z. S.; Howorka, S. Engineered Voltage-Responsive Nanopores. *Chem. Soc. Rev.* **2010**, *39*, 1115−1132.
(7) Guan, W.; Fan, R.; Reed, M. A. Field-Effect Reconfigurable Nanofluidic Ionic Diodes. *Nat. Commun.* **2011**, *2*, 506.
(8) Pérez-Mitta, G.; Albesa, A. G.; Trautmann, C.; Toimil-Molares, M. E.; Azzaroni, O. Bioinspired Integrated Nanosystems Based on Solid-State Nanopores: "Iontronic" Transduction of Biological, Chemical and Physical Stimuli. *Chem. Sci.* **2017**, *8*, 890−913.
(9) Wang, Y.; Chen, H.; Jiang, J.; Zhai, J.; You, T. Ion Transport Behaviors of Nanofluidic Diode Bichannel Systems in the Independent and Synergistic Cascade Mode. *ACS Appl. Mater. Interfaces* **2019**, *11*, 26467−26473.
(10) Ali, M.; Ramirez, P.; Nasir, S.; Cervera, J.; Mafe, S.; Ensinger, W. Ionic Circuitry With Nanofluidic Diodes. *Soft Matter* **2019**, *15*, 9682−9689.
(11) Zhang, P.; Xia, M.; Zhuge, F.; Zhou, Y.; Wang, Z.; Dong, B.; Fu, Y.; Yang, K.; Li, Y.; He, Y.; Scheicher, R. H.; Miao, X. S. Nanochannel-Based Transport in an Interfacial Memristor Can Emulate the Analog Weight Modulation of Synapses. *Nano Lett.* **2019**, *19*, 4279−4286.
(12) Kim, M. J.; Wanunu, M.; Bell, D. C.; Meller, A. Rapid Fabrication of Uniformly Sized Nanopores and Nanopore Arrays for Parallel DNA Analysis. *Adv. Mater.* **2006**, *18*, 3149−3153.
(13) Dekker, C. Solid-State Nanopores. *Nat. Nanotechnol.* **2007**, *2*, 209−215.
(14) Siwy, Z. S. Ion-Current Rectification in Nanopores and Nanotubes with Broken Symmetry. *Adv. Funct. Mater.* **2006**, *16*, 735−746.
(15) Lin, C. Y.; Wong, P. H.; Wang, P. H.; Siwy, Z. S.; Yeh, L. H. Electrodiffusioosmosis-Induced Negative Differential Resistance in pH-Regulated Mesopores Containing Purely Monovalent Solutions. *ACS Appl. Mater. Interfaces* **2020**, *12*, 3198−3204.
(16) Faucher, S.; Aluru, N.; Bazant, M. Z.; Blankschtein, D.; Brozena, A. H.; Cumings, J.; Pedro de Souza, J.; Elimelech, M.; Epsztein, R.; Fourkas, J. T.; Rajan, A. G.; Kulik, H. J.; Levy, A.; Majumdar, A.; Martin, C.; McEldrew, M.; Misra, R. P.; Noy, A.; Pham, T. A.; Reed, M.; Schwegler, E.; Siwy, Z.; Wang, Y.; Strano, M. Critical Knowledge Gaps in Mass Transport through Single-Digit Nanopores: A Review and Perspective. *J. Phys. Chem. C* **2019**, *123*, 21309−21326.
(17) Lan, W. J.; Edwards, M. A.; Luo, L.; Perera, R. T.; Wu, X.; Martin, C. R.; White, H. S. Voltage-Rectified Current and Fluid Flow in Conical Nanopores. *Acc. Chem. Res.* **2016**, *49*, 2605−2613.
(18) Yan, R.; Liang, W.; Fan, R.; Yang, P. Nanofluidic Diodes Based on Nanotube Heterojunctions. *Nano Lett.* **2009**, *9*, 3820−3825.
(19) Zhang, Z.; Wen, L.; Jiang, L. Bioinspired Smart Asymmetric Nanochannel Membranes. *Chem. Soc. Rev.* **2018**, *47*, 322−356.
(20) Pérez-Mitta, G.; Marmisolle, W. A.; Burr, L.; Toimil-Molares, M. E.; Trautmann, C.; Azzaroni, O. Proton-Gated Rectification Regimes in Nanofluidic Diodes Switched by Chemical Effectors. *Small* **2018**, *14*, 1703144.
(21) Zhang, S.; Yin, X.; Li, M.; Zhang, X.; Zhang, X.; Qin, X.; Zhu, Z.; Yang, S.; Shao, Y. Ionic Current Behaviors of Dual Nano- and Micropipettes. *Anal. Chem.* **2018**, *90*, 8592−8599.
(22) Laucirica, G.; Marmisollé, W. A.; Toimil-Molares, M. E.; Trautmann, C.; Azzaroni, O. Redox-Driven Reversible Gating of Solid-State Nanochannels. *ACS Appl. Mater. Interfaces* **2019**, *11*, 30001−30009.
(23) Rabinowitz, J.; Edwards, M. A.; Whittier, E.; Jayant, K.; Shepard, K. L. Nanoscale Fluid Vortices and Nonlinear Electro-osmotic Flow Drive Ion Current Rectification in the Presence of Concentration Gradients. *J. Phys. Chem. A* **2019**, *123*, 8285−8293.
(24) Kalman, E. B.; Vlassiouk, I.; Siwy, Z. S. Nanofluidic Bipolar Transistors. *Adv. Mater.* **2008**, *20*, 293−297.
(25) Lan, W. J.; Holden, D. A.; White, H. S. Pressure-Dependent Ion Current Rectification in Conical-Shaped Glass Nanopores. *J. Am. Chem. Soc.* **2011**, *133*, 13300−13303.
(26) Kowalczyk, S. W.; Wells, D. B.; Aksimentiev, A.; Dekker, C. Slowing Down DNA Translocation Through a Nanopore in Lithium Chloride. *Nano Lett.* **2012**, *12*, 1038−1044.
(27) Luo, L.; Holden, D. A.; Lan, W. J.; White, H. S. Tunable Negative Differential Electrolyte Resistance in a Conical Nanopore in Glass. *ACS Nano* **2012**, *6*, 6507−6514.
(28) Lu, B.; Hoogerheide, D. P.; Zhao, Q.; Zhang, H.; Tang, Z.; Yu, D.; Golovchenko, J. A. Pressure-Controlled Motion of Single Polymers Through Solid-State Nanopores. *Nano Lett.* **2013**, *13*, 3048−3052.
(29) Zeng, Z.; Yeh, L. H.; Zhang, M.; Qian, S. Ion Transport and Selectivity in Biomimetic Nanopores with pH-Tunable Zwitterionic Polyelectrolyte Brushes. *Nanoscale* **2015**, *7*, 17020−17029.
(30) Qiu, Y.; Siwy, Z. S.; Wanunu, M. Abnormal Ionic-Current Rectification Caused by Reversed Electroosmotic Flow under Viscosity Gradients across Thin Nanopores. *Anal. Chem.* **2019**, *91*, 996−1004.
(31) Garaj, S.; Hubbard, W.; Reina, A.; Kong, J.; Branton, D.; Golovchenko, J. A. Graphene as a subnanometre trans-electrode membrane. *Nature* **2010**, *467*, 190−193.
(32) Kowalczyk, S. W.; Grosberg, A. Y.; Rabin, Y.; Dekker, C. Modeling the Conductance and DNA Blockade of Solid-State Nanopores. *Nanotechnology* **2011**, *22*, 315101.
(33) Bu, Y.; Ahmed, Z.; Yobas, L. A Nanofluidic Memristor Based on Ion Concentration Polarization. *Analyst* **2019**, *144*, 7168−7172.
(34) Tsutsui, M.; He, Y.; Yokota, K.; Arima, A.; Hongo, S.; Taniguchi, M.; Washio, T.; Kawai, T. Particle trajectory-dependent ionic current blockade in low-aspect-ratio pores. *ACS Nano* **2016**, *10*, 803−809.

(35) Tsutsui, M.; Yokota, K.; Nakada, T.; Arima, A.; Tonomura, W.; Taniguchi, M.; Washio, T.; Kawai, T. Particle Capture in Solid-State Multipores. *ACS Sens.* **2018**, 2693−2701.
(36) Sun, G.; Slouka, Z.; Chang, H.-C. Fluidic-Based Ion Memristors and Ionic Latches. *Small* **2015**, *11*, 5206−5213.
(37) Sheng, Q.; Xie, Y.; Li, J.; Wang, X.; Xue, J. Transporting an Ionic-Liquid/Water Mixture in a Conical Nanochannel: a Nanofluidic Memristor. *Chem. Commun.* **2017**, *53*, 6125−6127.
(38) Sangwan, V. K.; Hersam, M. C. Neuromorphic Nanoelectronic Materials. *Nat. Nanotechnol.* **2020**, *15*, 517−528.
(39) Tsutsui, M.; Hongo, S.; He, Y.; Taniguchi, M.; Gemma, N.; Kawai, T. Single-Nanoparticle Detection Using a Low-Aspect-Ratio Pore. *ACS Nano* **2012**, *6*, 3499−3505.
(40) Lin, C. Y.; Chen, F.; Yeh, L. H.; Hsu, J. P. Salt Gradient Driven Ion Transport in Solid-State Nanopores: the Crucial Role of Reservoir Geometry and Size. *Phys. Chem. Chem. Phys.* **2016**, *18*, 30160−30165.

https://dx.doi.org/10.1021/acsami.0c15538
ACS Appl. Mater. Interfaces 2020, 12, 52175−52181